Impact of particle size distribution on the rest phase behavior of LIB cathodes – Model based analysis

Maximilian Fath [a,b,c,*], Peter Heidebrecht [a], Carsten Drechsler [a], Marc Kamlah [c]

[a] Center of Expertise of Reaction Engineering, BASF SE, 67056, Ludwigshafen, Germany
[b] Institute of Thermal Process Engineering, Karlsruhe Institute of Technology, 76131, Karlsruhe, Germany
[c] Institute for Applied Materials, Karlsruhe Institute of Technology, 76131, Karlsruhe, Germany

HIGHLIGHTS

- Modelling of effect of the particle size distribution on the rest phase potential.
- Investigation of the delayed voltage equilibration.
- Analysis of the apparent diffusivity in rest phase battery parametrization.
- Recommendations for the optimization of GITT experiments.

ARTICLE INFO

Keywords:
Lithium-ion nickel cobalt manganese oxide battery
NCM
Doyle-Fuller-Newman model
Particle size distribution (PSD)
Relaxation analysis
GITT

ABSTRACT

Dynamic measurements like the galvanostatic intermittent titration technique (GITT) and other pulse response measurements methods are widely used for the parametrization of battery and electrode models. These methods are based on the analysis of the transient cell potential in response to a change in the current. Most of them focus on the development of the cell potential as a current is applied to a formerly equilibrated cell. On the contrary, the interruption of the current and the development of the cell potential during the rest phase is more challenging to analyze. This is in parts attributed to the non-uniform particle size distributions of electrodes, while many analytical methods rely on the assumption of a single, representative particle size.

In this model study, we systematically analyze the impact of non-uniform particle size distributions by means of the extended Doyle-Fuller-Newman model. This is done both by analyzing varying distributions of discrete particle classes and comparing their effects on the voltage relaxation curve. From this, we derive recommendations for a more accurate design of relaxation experiments and provide a framework to interpret frequently observed deviations between electrochemical experiments and reduced order simulations.

1. Introduction

Due to the electrification of the transportation sector and the energy grid, as well as the growing market of handheld electronic devices, the requirements for the development of new batteries continuously increase. In particular, electromobility demands high charge rates, as well as high specific and volumetric energy densities.

Among the most promising cells for non-stationary devices are transition metal oxide cathodes combined with graphite or graphite/silicon blend anodes. Composite cathodes consisting of nickel, cobalt and manganese oxides (Li-NCM) have first been synthesized in 1999 by Liu et al. [1]. The capacity has been further improved over the years, by increasing the nickel content and reducing the amount of costly rare materials utilized, such as cobalt [2]. Other routes of cell optimization have been explored, too, such as the modification of the crystalline structure by dopants, the particle size distribution [3] and the mechanical processing of the cell [4].

While measuring the capacity and potential allows for a quick assessment of these cell modifications, a more in-depth understanding of the effects of these optimizations and the limiting processes can be attained using battery models. These range from 3D-resolved models on the scale of singular secondary particles to investigate the intercalation of Lithium ions in the solid phase [5], to reduced order models such as equivalent circuit models, suitable for application in battery

* Corresponding author. Center of Expertise of reaction engineering, BASF SE, 67056 Ludwigshafen, Germany.
E-mail address: maximilian.fath@basf.com (M. Fath).

management systems [6]. A widely used modelling tool of intermediate complexity is the homogeneous pseudo-2-dimensional (P2D) model for porous electrodes developed by Doyle, Fuller and Newman [7]. This approach homogenizes the pore space to improve the efficiency over 3D-resolved models, while preserving the physical description of the most relevant transport processes in both the electrode and electrolyte phases, as well as the electrochemical reaction.

The classical P2D-model assumes the presence of a uniform particle size distribution in the electrode, with all particles exhibiting the same spherical shape. In contrast to this, methods such as SEM-Imaging and laser diffraction show that both cathode and anode materials exhibit a wide range of particles sizes [8–10]. Consequently, a modification of the P2D-Model has been proposed by Ender to include a particle size distribution for graphite anodes [11]. The methodology is not limited to the anode and has been further extended to the cathode. This is shown in the work of Schmidt et al. [12] who compared the classic P2D model, the extended model as developed by Ender and spatially resolved 3D-models.

A prerequisite for the proper application of such models is their accurate parametrization. This requires multiple dedicated experiments, as solely fitting charge- and discharge profiles is not sufficient to distinguish between the various dynamic processes. This has been shown by Laue et al. [13] for the solid diffusivity and the exchange current density, elucidating the ambiguity of the parameters. One of the dynamic method commonly used in addition to charge- and discharge profiles is the galvanostatic intermittent titration technique (GITT). This was first proposed by Weppner et al. [14], for non-porous electrodes. It is based on the dependency of the electrode potential on the concentration of intercalated ions on the particle surface, described by the open circuit voltage (U^{OC}). In combination with Fick's law, a diffusion flux within the material can therefore be correlated to a change in the surface potential.

Despite the widespread use of this method to determine kinetic and transport parameters, the reported results vary widely for a given material. This has been summarized in a recent work by Kang et al. [15], which names possible sources for deviation of the diffusion coefficients and discuss challenges stemming from porous electrodes. In particular due to the composition dependency of the reaction overpotentials, it was concluded that an evaluation of the rest phase instead of the current phase may improve reproducibility.

More recent works have focused on evaluating the rest phase or combining current and rest phase in order to quantify cell properties. The intermittent current interruption (ICI) developed by Chien et al. [16] analyses the gradient of the potential curve for a period of up to 10 s after the interruption of the current. The analysis is based on similar evaluation principles as the classical GITT by Weppner. A more in-depth approach has been utilized by Horner et al. [17], where a single particle model for a porous FeS_2 electrode has been fitted to both charge and relaxation phases of a GITT-pulse. A similar approach has been used by Dees et al. [18], in which a P2D-Model has been fitted to the current and rest phase of a GITT-cycle obtained for a lithium nickel cobalt aluminum oxide cathode. Despite both models yielding high agreement between experimental and simulated data, a systematic error in the form of an unexpected signal tailing of the experimental cell potential has been observed. Consequentially, the simulated curves cannot fully reproduce the shape of the experimental data. This delayed relaxation of the experiment compared to the model has been investigated by Kirk et al. [19] for the voltage relaxation at the end of a full discharge. The work utilized an extended P2D-Model for non-uniform particle size distributions, similar to the model developed by Ender. Furthermore, both the particle size distribution and the diffusion coefficient have been adjusted to increase the accuracy of the model compared to the verification experiment done by Chen et al. [8].

In this work, we go beyond the contributions of Kirk and Dees, by systematically investigating the impact of particle size distributions on the cell potential during a GITT rest phase. Moreover, we provide a framework for the design of experiments and interpretation of deviations between idealized models and experiments.

In Section 2, the physico-chemical processes during the rest phases in cathodes with non-uniform particle size distribution are introduced, and the extension of the P2D-Model is described. Furthermore, the simulation assumptions for the particle size distribution and U^{OC} are discussed, with the results being presented in Section 3. In Section 4, we derive conclusions for intermittent electrochemical experiments and discuss the apparent diffusivity stemming from GITT-Experiments.

2. Methods and background

2.1. Relaxation processes in porous electrodes

Due to the few measurable cell properties, a core concept to the analytics of batteries is the investigation of dynamic processes on variable time scales. Prior to introducing mathematical equations, a common understanding of the physical and chemical processes in a cathode following a current interruption is required. We will discuss these for an idealized cathode first, followed by the impact of spatial distribution and non-uniform particle size distribution on these processes.

For illustrative purposes, the process is elaborated for a current interruption following a galvanostatic charge phase, but similar processes occur for any change in the current. The idealized cathode in this example is a single, spherical particle. At the end of the charging period, when the current is set to zero, the following processes occur [20].

1. Due to the high mobility of electrons in the solid, the potential gradient in the solid equilibrates nearly instantaneously with the interruption of the current.
2. The flux of ions towards the particle surface is interrupted and the polarization of the double layer between solid and liquid approaches equilibrium, bringing the reaction rate to zero. This effect correlates with the double layer capacity and is considered to happen in the timeframe of seconds.
3. The radial concentration profile of intercalated lithium ions in the electrode particles equilibrates. This process is dependent on the ion mobility in the solid. Under the given, idealized circumstances, the particle approaches equilibrium after hours.

This idealized concept is the standard assumption for commonly used relaxation experiments, including GITT, which more closely investigates the third step. For modelling purpose, this idealized situation is equivalent to the assumptions of single particle models, which are widely used to estimate the state of charge and state of health of batteries [21,22].

However, additional complexity is added due to the spatial distribution of particles along the electrode depth. For higher currents, a significant concentration profile of solvated ions is formed in the electrolyte phase. Both the magnitude of the gradient during the charge phase, as well as the time required for the equilibration, depend on the tortuosity of the cell and diffusivity of solvated ions within the electrolyte. Consequentially, as the exchange current density is a function of salt concentration in the electrolyte, c^{E}, and of the lithium ions on the particle surface, c^{S}_{Surf}, (See Appendix A for equations), the extent of the intercalation and extraction of ions varies over the depth of the electrode. This results in an increased reaction rate closer to the separator, and therefore different lithiation of the particles. High currents, thick electrodes and high tortuosity caused by dense particle packing further exacerbate this non-uniformity.

This heterogeneity of the surface concentration at the beginning of the rest phase further leads to a deviation in the electrochemical potentials on the surface of the particles. More specifically, the local gradient of the U^{OC} - curve translates the concentration difference between particles at different positions to differences in the ~.

electrochemical potential, providing a driving force for the equilibration. These processes are already included in the classical P2D-model [7].

If particles of different radius or shape – and, therefore, of different specific surface – are present in the electrode, a further source of heterogeneity is introduced. Smaller particles will exhibit more extreme states of charge or depletion, as well as shorter solid diffusion pathways that allow for faster equilibration. Larger particles show more moderate changes in their states of charge relative to the initial state, due to their lower surface to volume ratio and longer diffusion pathways. This is depicted in Fig. 1, showing the current and rest phase for an exemplary charge process. In comparison, the uniform particle size distribution (uPSD) exhibits only an equilibration along the radius, while a cascade of processes can be seen for non-uniform particle size distributions.

Under charging operation, e.g. the extraction of Li-ions from the cathode, the smallest cathode particles reach the lowest average concentration. This is due to the higher specific surface, and therefore higher intercalation flux. Larger particles show an overall higher concentration after the current phase. Following the current interruption, the smallest particles are the first to attain equlibrium along the radial coordinate, but this state of uniformity still exhibits a lower concentration than the average concentration in all particles of the electrode. As seen in the intermediary step in Fig. 1, as the larger particles equilibrate and the concentration of lithium ions on the surface increases beyond the near-equilibrium concentration of the smaller particles, they will extract additional lithium ions, filling the smaller particles. This continues until all particles exhibit a homogenous concentration independent of their size.

Thus, it can be concluded that the time required for equilibration as well as the magnitude of the surface concentration variation, and therefore the potential evolution during the relaxation period, depends on the particle size distribution. Further influences are the current magnitude and duration of the preliminary charging period, and the local gradient of the U^{OC}-Curve.

2.2. Model description

The model used in this work is based on an extension of the classical P2D model, which will be introduced first. Following this, the modifications necessary to include a non-uniform particle size distribution are outlined.

The core idea of the P2D model is the homogenization of the electrode from an assembly of discrete particles to a continuous, porous structure on the cell level. The transport within the solid electrode particles is modelled in representative spheres, using Fick's law. The two dimensions are connected by the intercalation/extraction ion fluxes. These are the microscopic current densities calculated via the Butler-Volmer-Equation, scaled with the specific surface area of the particles. The full model equations are outlined in Appendix A. Hereafter, the macroscopic dimension along the depth of the cell, spanning between the current collectors will be referred to as the z dimension, and the microscopic scale within the particles as the r dimension.

The P2D model has been extended by the work of Ender [11], in order to account for non-uniform size distribution of spherical particles. The model still assumes homogeneity, with no further changes to the calculation along the z dimension. On the particle scale, particles of different sizes are considered to independently co-exist with a given mass fraction. Solid-to-solid transport of ions is not modelled, as the transport throughout the electrolyte is dominant. Contrary to the classical P2D model, the change in the cell current and ion flux along the electrode depth (1) is calculated as the sum of the microscopic reaction current density j for a given particle size class m, multiplied with the specific surface of that class a_m. For spherical particles, the surface of the individual classes can be calculated from the particle radius, r_m, weighted with the mass fraction of the particle class, w_m, and with the overall porosity of the solid, ε.

$$\frac{\partial i}{\partial x} \quad \sum_{m\ 1}^{n_y} j_m \bullet a_m \quad \sum_{m\ 1}^{n_y} j_m \bullet \frac{3}{r_m} \bullet (1 \quad \varepsilon) \bullet w_m \tag{1}$$

The model equations have been solved by discretization using the Finite-Volume-Method along z and r. The implementation has been done in MathWorks MATLAB R2022B, using the variable time-step ode15s-Solver for stiff systems. 21 discretization steps have been used along z in anode, cathode, and separator each, and 30 discretization steps along r. A further reduction in discretization volume size did not affect the results in an observable manner. Values for the initial potential jump within the liquid and solid at the start of each current and rest phase have been calculated by using a sigmoid function between the current of the previous and next phase, in order to improve numerical stability.

The parameter set is taken from the publication by Chen et al. [8] in which NCM811 extracted from commercial LG M50 cells has been characterized using EIS and GITT measurements. The parameter set is summarized in Appendix B. Both this reference work as well as fundamental studies on NCM-Materials strongly suggest that the diffusivity is dependent on the state of charge. This is effect is most pronounced for very high and low degrees of lithiation [23,24]. Within this work, it is assumed to be constant, as only mid-range stoichiometries are investigated.

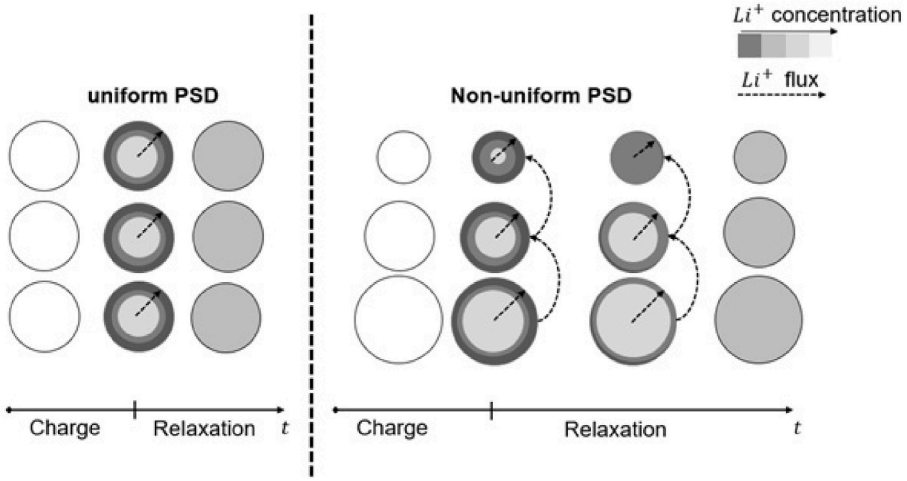

Fig. 1. Schematic of the relaxation during the rest phase for uPSD and non-uniform PSD electrode before the charge phase, at the end of the charge phase and during the relaxation. Darker shades of Grey indicating lower Lithium ion concentration, dashed arrows showing lithium ion flux directions.

Furthermore, the anode has been simplified to isolate the effects of the cathode by assuming a solid potential of near zero and the overpotentials of the anode have been subtracted from the cell potential.

2.3. Simulation of the rest phase

2.3.1. Investigation of the local U^{OC}-gradient

As explained in the previous section, the U^{OC} curve and especially the gradient of U^{OC} are expected to play a key role in the rest phase behavior of electrodes. In order to obtain realistic values for the gradient, the NCM 811 U^{OC}-Curve from the work by Chen et al. [8] is used as reference (2).

$$U^{OC}(x) \quad 0.809\,x + 4.4875 \quad 0.0428 \bullet \tanh(18.5138(x \quad 0.5542)) \quad 17.7326 \bullet \tanh(15.7890(x \quad 0.3117)) + 17.5842 \bullet \tanh(15.9308(x \quad 0.3120)) \tag{2}$$

The magnitude of the first order derivative ranges from 10 to 40 $\mu V\,m^3\,mol^{-1}$ within the standard operation range of the cell. Four values across this range were selected for calculation purposes (Table 1). In the following simulations, the local U^{OC} curve is approximated as a linear correlation for the given range. This is due to each charge phase in GITT only leading to a small change in the overall concentration and therefore spanning over a small part of the U^{OC} curve.

To analyze the impact of the local U^{OC}-gradient on the relaxation behavior, a reduced particle size distribution will be used (PSD A in Table 2, discussed in Section 2.3.2). Additionally, the case of an idealized phase change in the solid is included, with a gradient of near zero, where a non-zero value has been chosen for reasons of numerical stability.

2.3.2. Effect of the particle size distribution

The particle size distribution presented by Chen et al. [8] will be used as a basis for this work. Following this, all additional particle size distributions defined in this work show a similar tailing towards larger particles sizes instead of symmetric behavior.

As the purpose of this work is the investigation of principal effects of different particle sizes, the derived particle size distributions are simplified, to improve intuitive understanding of the results. In the first step, the effect of this simplification is investigated. This is done by comparing the voltage relaxation of the highly resolved non-uniform particle size distribution provided by Chen et al. [8] with particle size distribution of decreased resolution, down to uniformity. This comparison will show that a particle size distribution with only 3 particle classes is sufficient to qualitatively reflect the effects observed with a complete distribution. Thus, simulations for the comparison of different types of non-uniform particle size distributions will solely be utilizing simplified distributions (Table 2).

PSD A is oriented on the rounded 10th and 90th percentile of the fully resolved particle size distribution, with only small amounts of smaller and larger than median particles. It will be used as reference throughout this work. PSD B shows the same 3 radii but has a higher content of smaller and larger particles, comparable to a wider particle size distribution. PSD C represents a bimodal particle size distribution as used in the production of high capacity cells [3]. PSD D represents a very narrow particle size distribution, and E is comparable to C, with the bimodal size classes being closer to each. In the following, the class of smallest particles will be referred to as R_{min}, the particle class of median size as R_{med}, and the class of the largest size particles as R_{max}.

Table 1
Linearized U^{OC} gradients used for calculations of the deviation of the relaxation phase potential based on the U^{OC} Curve of NCM 811.

$\frac{dU^{OC}}{dc}/\frac{\mu V m^3}{mol}$
−10 [10]
− 10
− 20
− 30
− 40

Table 2
Simplified particle size distribution for the voltage relaxation.

Particle size	PSD A w%	PSD B w%	PSD C w%	PSD D w%	PSD E w%
0.5 R_{med}	10	20	50		
0.75 R_{med}				10	50
1.0 R_{med}	80	60		80	
1.5 R_{med}				10	50
2.0 R_{med}	10	20	50		

The different simulations are conducted under the assumption that the particle size distribution has no effect on the transport within the liquid phase. Especially for larger currents and limitation within the transport of the solvated ions, this may not be valid, as both tortuosity and porosity heavily depend on the particle size distribution. Further investigation into this would require experimental measurements or 3D simulations, which will be investigated in detail in a follow-up paper.

2.3.3. Quantification of the rest phase potential deviation

All simulations in this work are based on a galvanostatic charge phase of 1000 s length at 0.3 C (13.44 A/m^2) for the given cell thickness and an arbitrary cell size, followed by a relaxation phase of up to 4 h length. The C-rate is defined relative to the capacity of the cathode with the given upper and lower limits of stoichiometry given in Appendix B. The initial, uniform stoichiometry at the start of the charge phase is chosen at 0.554, such that all cases reach an average lithium ion stoichiometry of 0.5 after the above-mentioned charge phase.

Furthermore, we define the difference in rest phase potential between simulation assuming a uniform particle size distribution and one using a non-uniform particle size distribution, ΔE as metric.

$$\Delta E \quad U_P^{PSD} \quad U_P^{uPSD} \tag{3}$$

Graphical representations of the rest phase potentials and ΔE are depicted in Fig. 2 (a) and (b) respectively. Both simulations with uniform and non-uniform particle sized distribution are carried out at the same local U^{OC} gradient.

When comparing the potential responses following the current interruption, a time dependent deviation caused by the PSD can be observed. Throughout the following sections, the magnitude and shape of the deviation ΔE will be used as a measure of the impact of the PSD and the local U^{OC} gradient. For practical application, ΔE corresponds to a systematic error in rest phase analysis methods.

3. Results

3.1. General effects of the particle size distribution

In the following, the interactions between particles of different sizes, introduced in Section 2, will be discussed. This will be shown exemplarily for a simplified electrode consisting only of 3 discrete particles classes. The effects and limitations of this simplification will then be discussed in the following Section 3.2.

Fig. 3(a–c) shows the Lithium content in particles of different sizes, at various radial positions. All particles are located at the mid-depth of the cathode. (a) depicting the smallest class of particles, (b) the median class and (c) the largest class. In each diagram, the lithium-ion stoichiometry at the surface is shown, together with the content at the particle center, and a volume averaged lithium-ion stoichiometry of that particle class. In addition, Fig. 3(d) shows the reaction overpotentials at the surface of each particle class during relaxation.

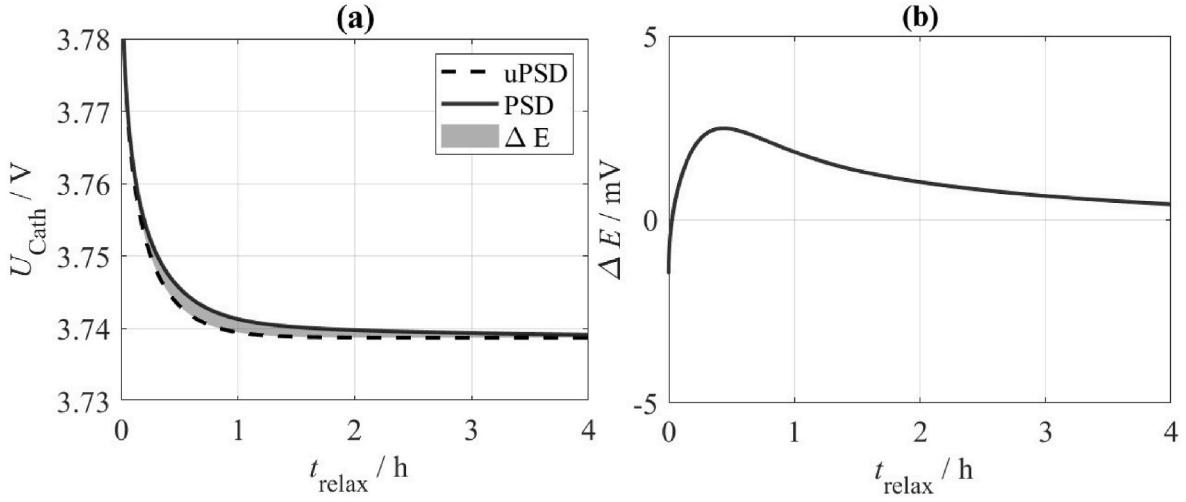

Fig. 2. (a) Exemplary rest phase following a 0.3 C Charge phase for 1000 s and a local U^{OC} gradient of 20 μV m^3 mol^{-1}. Dashed line: cathode potential response for uPSD, Solid line: Cathode potential response for PSD A. Grey shaded area: Deviation ΔE. (b) ΔE over the relaxation period.

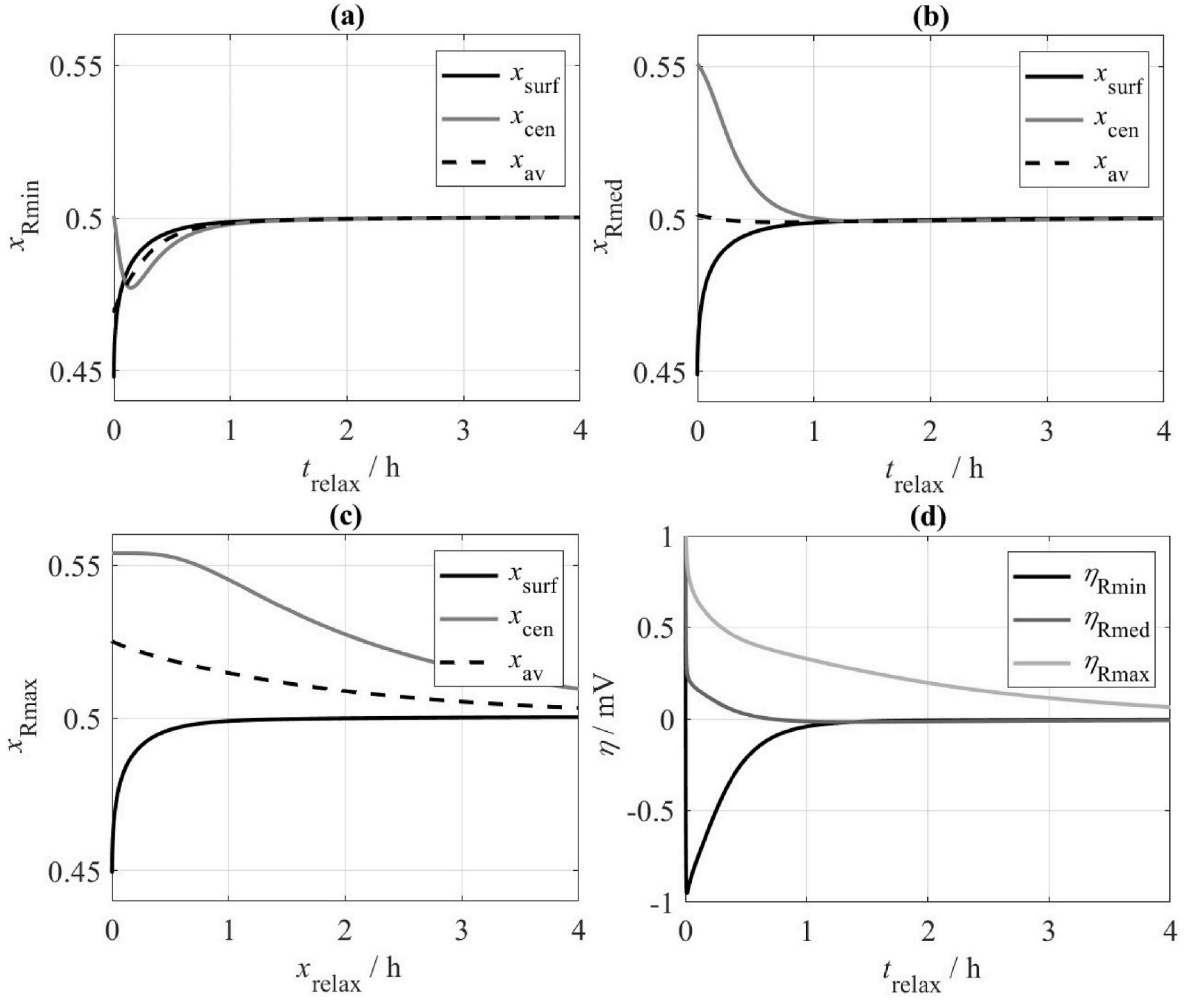

Fig. 3. Surface, center and volume average Li^+ stoichiometry and reaction overpotential during rest phase following a 0.3 C Charge process for 1000 s/0.3 C at 20 μV m^3 mol^{-1} U^{OC} -gradient with PSD A. (a) R_{min} particle class. (b) R_{med} particle class. (c) R_{max} particle class. (d) Reaction overpotential on the particle surface of different particle sizes.

Initially, at the interruption of the current, all particles show a similar surface lithium-ion stoichiometry, with a negative gradient from center to surface. The R_{min} particle class shows the overall lowest content of lithium, as well as the lowest diffusion pathway length. Consequentially, the equilibration along the radial coordinate is finished after a few minutes, after which the gradient inverts, indicating an intercalation of

lithium into the particle, Fig. 3(a). In parallel, both the R_{med} and R_{max} particle classes are reduced in their average concentration, Fig. 3(b) and (c). After 1 h, R_{min} and R_{med} are in equilibrium along their radial coordinates, and relative to each other. In the following, both only show a slight increase over time, due to the R_{max}, which exhibits a higher average lithium-ion content, diminishing over time. After 4 h, the R_{max} particles are not in equilibrium along the radius, and continuously extract lithium ions into the R_{med} and R_{min} particle class.

This is further exemplified by the reaction overpotential in Fig. 3(d), with positive overpotentials signifying the extraction of lithium-ions into the electrolyte, and negative overpotentials the intercalation into the solid. R_{min} particles show a minimum potential in the beginning, as strong transport between R_{min} and R_{med} particles takes place, with the mass fraction of R_{med} particles being 8 times higher. During later times, small quantities of R_{max} particles extract lower amounts of lithium into the smaller particles, with a proportionally higher overpotential due to the lower specific surface area of the R_{max} particles.

3.2. Impact of the PSD resolution

At first, we investigate the impact of the resolution of a particle size distribution on the ΔE. The reference by Chen [8] describes 12 particle classes, with a resolution of 1 µm. In a first step, the discrete classes have been combined into 6 classes of 2 µm resolution. This has been further reduced into 3 classes and rounded up, resulting in PSD A in Table 2.

In Fig. 4(a), the difference in relaxation voltage between a fully resolved particle size distribution and a uniform particle size distribution is depicted. Two characteristic regions are shown. Initially, the assumption of a uniform particle size distribution overestimates the relaxation voltage, later underestimating it. This can be further seen in Fig. 4(b), which shows a large negative ΔE in the beginning for all resolutions. Later, ΔE increases, forming a peak after 1 h, and then asymptotically approaching 0.

The shape of the curve can be directly correlated with the processes describe in the previous chapter. The initial decrease in voltage of the non-uniform PSD is due to the readily available lithium ions in small particles at short diffusion pathways, mediating the surface stoichiometry of all particle classes. At later times, the relaxation is delayed due to the slow diffusion in large particles. The peak of ΔE at 1 h is due to the buffering effect of both processes overlapping, drastically reducing the relaxation curve gradient.

This general shape can be seen both in fully resolved particle size distributions, as well as in reduced ones. The reduction leads to a shift in the position of the maxima of the ΔE curve. A reduction to 6 classes shows a shift to slightly higher deviations at lower times, and 3 classes to a further increase in ΔE and a shift to longer times. This is in particular due to the lacking resolution in the middle range of particle sizes, and deviations due to rounding of the 10th and 90th percentile.

In conclusion to this, the reduced PSD A to E as seen in Table 2 will be used throughout this work for the intuitive understanding, as it allows to elucidate all main interactions between particle classes during the relaxation. Furthermore, the reduction is feasible for the investigation of the long-term relaxation, as only the largest particle classes influence this. Contrary, to accurately simulate the relaxation curve over the full relaxation time, and in particular the initial impact of smaller particles and the ΔE peak, a higher resolution is necessary, as done in the later simulations of the apparent diffusivity.

3.3. Impact of the U^{OC} – gradient on the rest phase potential

As the U^{OC} gradients determine the deviation in potential between particles of different Li^+-content, the impact is investigated using the different locally linearized U^{OC} gradients according to Table 1. Fig. 5 shows the potential deviations ΔE for different U^{OC} gradients.

For a near-constant U^{OC}, the rest phase voltage following a current interruption with uniform and non-uniform PSD are identical within the numerical accuracy. Under these circumstances, the varying surface concentrations have no impact on the electrochemical potential. Thus, no driving force for the exchange of lithium ions is present, with no equilibration in between particles of different size is taking place. For non-zero gradients, the curves show the same general shape as seen in Section 3.2, with negative initial values, a maximum during the first hour and asymptotic decrease towards 0, Fig. 5(a). When normalizing the ΔE curves with ΔE stemming from an U^{OC}-gradient of 40 µVm^3 mol^{-1}, the shape of the deviation is widely independent of the U^{OC} -gradient, Fig. 5(b). At low times, the ΔE curve shows a zero intersection, strongly amplifying deviations between the U^{OC}-gradients. In consequence, despite the U^{OC}-gradient providing the driving force for the equilibration, the time-limiting process is the transport in the solid, which, in this example, is independent of the electrical potential of the surface.

3.4. Impact of the particle size distribution on the rest phase

Based on the results in Section 3.2, a U^{OC}-gradient of 20 µV m^3 mol^{-1} is used for the investigation of the impact of the particle size distributions given in Table 2, Fig. 6. The cell parameters and the parameters of the charge phase remain unchanged.

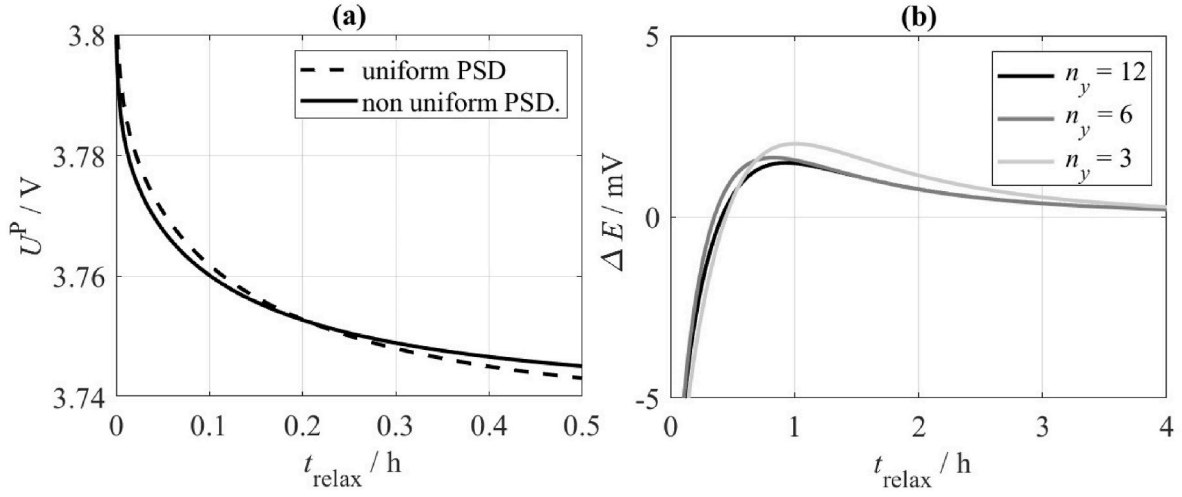

Fig. 4. Rest phase potential following a 0.3 C Charge process for 1000 s at 20 µV m^3 mol ^{1} U^{OC} -gradient. (a) Relaxation potential of a fully resolved non-uniform PSD (solid line) compared to uniform PSD (dashed line) throughout the first 0.5 h. (b) ΔE for varying resolutions of non-uniform PSD.

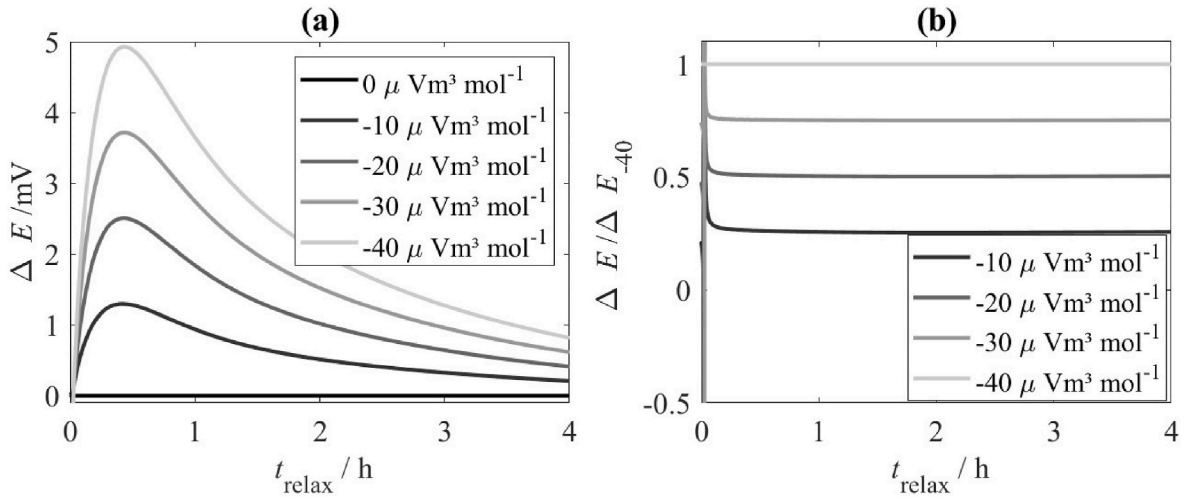

Fig. 5. Rest phase potential of a P2D Model with PSD following a 1000 s/0.3 C charge phase of NCM 811 with PSD A and linearized U^{OC} gradient ranging from 0 to 40 μVm^3 mol ^{1}. (a) Deviation between uniform- and non-unform particle size distributions ΔE. (b) ΔE normalized with the ΔE at 40 μVm^3 mol ^{1}.

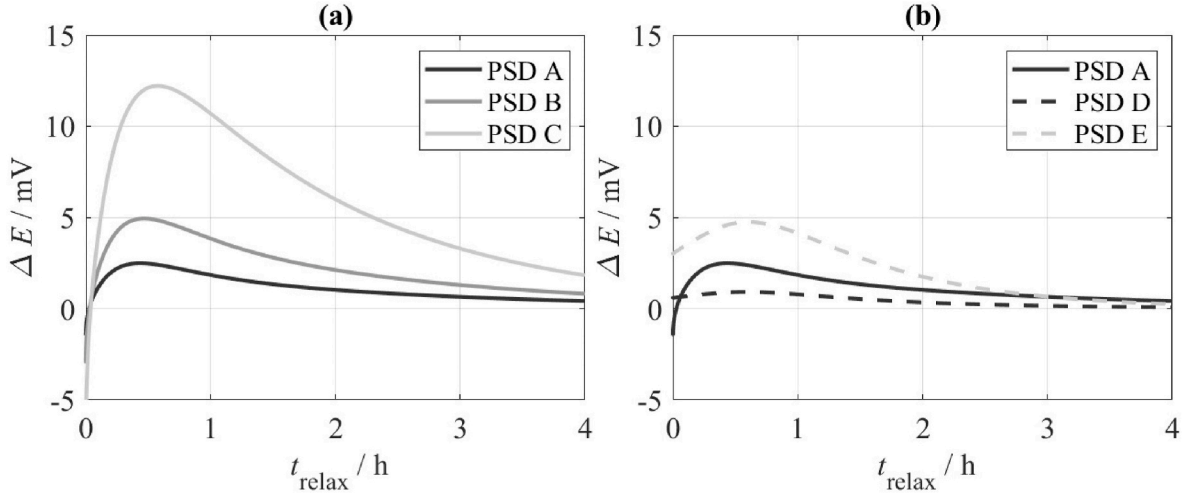

Fig. 6. Effect of the particle size distribution on the rest phase potential following a 1000 s/0.3 C charge process for at 20 μV m^3 mol ^{1} U^{OC}- gradient. (a) Variation of mass fraction of particles of 50 % and 200 % of R_{med} (10, 20, 50 % volume fraction each). (b) Variation of the mass fraction of particles of 75 % and 150 % of R_{med} (10, 50 % volume fraction each) versus the reference PSD A.

Fig. 6 gives an overview over the results of the deviation caused by different non-uniform particle size distributions. In Fig. 6(a), three more wide-spread particle classes are compared, and the following observations can be made.

- The reference, PSD A, is set to be identical to 20 μV m^3 mol^{-1} in Fig. 5.
- Increased amounts of smaller and large particles, PSD B, result in a significant increase in the maximum deviation between uniform PSD and non-uniform PSD compared to PSD A, more than doubling it from 2.3 to 5 mV. Similarly, the negative starting point is decreased due to the larger fraction of smaller particles, with the potential starting out at 3 mV.
- The bimodal distribution, PSD C, Continues the trend, starting out at a lower point and reaching a higher peak. After 4 h, the electrode still shows a significant deviation, showing a residual Δ*E* of approximately 2 mV after 4 h.

In Fig. 6(b), the same comparison is shown for particle classes closer to the median, with PSD A added as a reference.

- Closer to median particle sizes, PSD D, show no initial negative values, as both the stoichiometry of particles of different sizes and the diffusion pathways are more moderate. As Fickian diffusion scales with the diffusion pathway squared and the specific surface linearly inverse, the equilibration along the radial coordinate is not as fast as in PSD A. Therefore, the small particles are not capable of mediating the surface lithium ion stoichiometry to the extend seen before. Furthermore, due to the lower size of the largest particle class, the cathode approaches zero Δ*E* after approximately 3 h.
- The bimodal distribution of closer to median particles, PSD E, exhibits a comparable peak height as PSD B, approximately 5 mV, but further shows no negative starting values and falls below PSD A's Δ*E* after 3.5 h.

The comparison of PSD A versus PSD E shows that small amounts of particles of twice the median size lead to higher residual Δ*E* after 4 h, compared to large quantities of particles with 150 % the median radius. Similarly, particles of half the median radius result in a more negative Δ*E* in the beginning, while large quantities of 75 % radius particles show no negative Δ*E*. Therefore, it can be concluded that the limiting process on long time frame is the diffusion in the solid within R_{max} particle class,

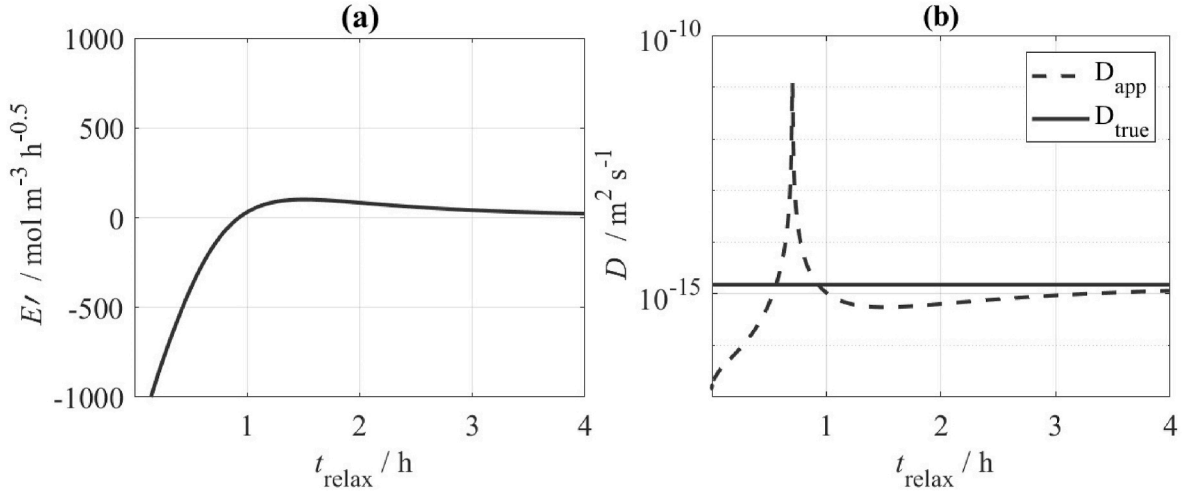

Fig. 7. (a) the derivate deviation between uniform and non-uniform PSD E' following a 0.3 C charge process for 1000 s/0.3 C for PSD A. (b) Apparent diffusivity for relaxation GITT for uniform- and non-uniform particle size distributions.

not the amount of lithium ions exchanged. This further supports the conclusion of the previous section regarding the U^{OC}-gradient. These findings are in agreement with the fundamental results by Kirk et al. [19], which attributed the increased tailing, and therefore time required for voltage relaxation, to a more widespread particle size distribution. In addition, our results further show that outliers, small fractions of extraordinary large or small size, may be dominant during relaxation, independent of the overall shape of the PSD, and need to be considered for relaxation experiments.

4. Discussion

4.1. Impact of non-uniform particle size distribution on relaxation GITT

The classical GITT according to Weppner [14] has been developed for the charge phase, but variations of the method have been adapted for the relaxation phase. This has been done by the work of Kang et al. [15] or the ICI developed by Chien et al. [16].

A principal aspect of the original derivation by Weppner was the assumption of a non-porous electrode, or a singular electrode particle. Going back to Section 2, it can be seen that this omits two relaxation processes in porous electrodes. These being the equilibration among the spatial coordinate, and the interaction between particles of different sizes. In this section, we will discuss the estimation error created by applying the method by Weppner to such a non-ideal electrode.

The evaluation will be carried out based on Equation (3), the definition of the deviation between uniform and non-uniform particle size distributions. Based on Fig. 5(b), it can be assumed that the local U^{OC} gradient has no effect on the time dependency of the deviation for most of the relaxation duration, only on the magnitude. Therefore, the deviation is split into a base function E and the U^{OC}-gradient (4).

$$U_{PSD} \quad U_{uPSD} \quad \Delta E \quad E \cdot \frac{dU^{OC}}{dx} \tag{4}$$

E is a function of the shape of the particle size distribution, as well as the time and the initial state of non-equilibrium following the current phase. This can be formally derived by the square root of time to obtain equation (5).

$$\frac{dU_{PSD}}{d\sqrt{t}} \quad \frac{dU_{uPSD}}{d\sqrt{t}} \quad \frac{d\Delta E(t)}{d\sqrt{t}} \quad \frac{dE}{d\sqrt{t}} \cdot \frac{dU^{OC}}{dx} \quad E' \cdot \frac{dU^{OC}}{dx} \tag{5}$$

The same combination of the derivate of the voltage over time and U^{OC}-gradient can be seen in the evaluation equation for the GITT as derived by Weppner [14]. The general shape of the evaluation equations for the apparent diffusivity D_{app} consists of a constant coefficient including cell geometry, material constants and experimental conditions, which are gathered in the constant K_W. The second term contains the derivative of the experimental potential U_{exp} along the square root of the time, normalized with the U^{OC} gradient.

$$D_{app} \quad K_W \left(\frac{\frac{dU_{exp}}{d\sqrt{t}}}{\frac{dU^{OC}}{dx}} \right)^2 \sim D_{app} \quad K_W \left(\frac{\frac{dU_{PSD}}{d\sqrt{t}}}{\frac{dU^{OC}}{dx}} \right)^2 \tag{6}$$

For this evaluation, it is assumed that the experimental voltage relaxation can be approximated by the simulated voltage relaxation of a non-uniform PSD electrode U_{PSD}. Furthermore, the spatial distribution within the uniform particle size distribution is neglected, as it is assumed that the current is sufficiently low, and the gradient within the electrolyte neglectable.

By combining equations (5) and (6), the voltage relaxation of an electrode with non-uniform particle size distribution can be reformulated into the response of a uniform particle size electrode U_{uPSD} and E' (7).

$$D_{app} \quad K_W \left(\frac{\frac{dU_{PSD}}{d\sqrt{t}}}{\frac{dU^{OC}}{dx}} \right)^2 \quad K_W \left(\frac{\frac{dU_{uPSD}+d\Delta E}{d\sqrt{t}}}{\frac{dU^{OC}}{dx}} \right)^2 \quad K_W \left(\frac{\frac{dU_{uPSD}}{d\sqrt{t}} + E' \frac{dE^{OC}}{dx}}{\frac{dU^{OC}}{dx}} \right)^2 \quad K_W \left(\frac{\frac{dU_{uPSD}}{d\sqrt{t}}}{\frac{dU^{OC}}{dx}} + E' \right)^2 \tag{7}$$

By splitting up the bracketed term, the apparent diffusivity, D_{app}, can be calculated from the true diffusivity, D_{true}, which can be derived by the GITT-Evaluation of a hypothetical single particle system and E',

Table 3
Particle Size distributions and diffusion times for the study of the equilibration and characteristic diffusion times for a diffusion coefficient of 1.5·10^{-15} m^2/s.

R_{max}	1.0 R_{med}	1.4 R_{med}	2.0 R_{med}	2.5 R_{med}	3.2 R_{med}
$t_{D,R_{max}}$/h	6.25	12.4	25.0	39.1	62.

Equation (8).

$$\frac{1}{\sqrt{D_{\mathrm{app}}}} \quad \frac{1}{\sqrt{K_w}}\left(\frac{\frac{\mathrm{dU_{uPSD}}}{\mathrm{d}\sqrt{t}}}{\frac{\mathrm{dU^{OC}}}{\mathrm{dx}}}+E^{'}\right) \quad \frac{1}{\sqrt{D_{true}}}+\frac{E^{'}}{\sqrt{K_{\mathrm{W}}}} \tag{8}$$

In the following, the magnitude of $E^{'}$ over the relaxation time is shown, as well as the apparent diffusivity. $E^{'}$ and the apparent diffusivity have been calculated from a simulated voltage relaxation following a 1000 s charge phase at C/3, using the fully resolved particle size distribution by Chen et al. [8].

$E^{'}$ in Fig. 7(a) starts out at a low negative value after the current interruption, rising significantly during the first hour and showing a zero intersection. Later, the values remain positive, asymptotically approaching 0 over the relaxation time. The apparent diffusivity in Fig. 7(b) is initially orders of magnitude below the true value, rapidly increasing. After half an hour, the apparent diffusivity is as large as the real diffusivity. Afterwards, the apparent diffusivity shows a peak, followed by a drop to negative values, from where it asymptotically approaches the true value of the diffusivity. After 4 h, the apparent diffusivity is $1.15{\cdot}10^{-15}$ $\mathrm{m^2/s}$, vs. a true value of $1.5{\cdot}10^{-15}$ $\mathrm{m^2/s}$, resulting in an error of 24 % in this example.

The irregular shape of the apparent diffusivity can be explained due to the interactions of particles of different sizes. Initially, all particles show similar surface concentrations, but vastly different bulk concentrations. Among them, the smallest particles have the lowest bulk concentration and shortest diffusion pathway length.

Consequentially, the surface stoichiometry of the smaller particles increases due to radial equilibration and does so faster than in larger particles. As the kinetics are considered to be faster than the diffusion, the smaller particles exchange ions with larger ones, increase their surface concentration and reduce their U^{OC}. This has been shown in Section 3, with the initial negative ΔE.

After the concentration gradient within the smaller particles have flipped, e.g., a positive gradient from center to surface has been established and lithium ions are intercalated, the lithium ions on the surface of larger particles are depleted. Due to the longer diffusion pathways in larger particles, the lithium ions are more slowly refilled from the particle bulk. This buffering system of particles of multiple sizes leads to a moderation of the voltage relaxation gradient. Due to this, the apparent diffusivity is drastically overestimated.

During this, the non-uniform particle size distribution electrode approaches the relaxation gradient of a single particle, resulting in the zero intersection in the diffusivity. After approximately 1 h, the zero intersection in $E^{'}$ occurs, at the same time as the maximum of ΔE in Fig. 3(b). During this, small and medium particle classes are widely in equilibrium concerning their radial concentration, and the overall equilibration becomes increasingly limited by the larger particles. The apparent diffusivity decreases, leading to another zero-intersection in the diffusivity, followed by an underestimation of the diffusion coefficient.

4.2. Application in experimental design

In the following, recommendations for the design of parametrization experiments, based on the modelling results in the previous sections, are given. This includes both rest phase analysis, as well as the corresponding conclusions for current phase analysis.

A. Particle size distribution

The particle size distribution has a significant influence on the shape of the relaxation curve, with smaller particles dominating the relaxation on a short time scale, and large particles dominating the long-time behavior. Section 4.1 shows that the apparent diffusivity reaches the true value at two points during the early relaxation, but these cannot be determined within an experiment. Therefore, the value of the apparent diffusivity is best determined at the longest possible relaxation time, with respect to the signal-to-noise ratio of the experiment.

Furthermore, the error is reduced by narrower particle size distributions, as shown in this work via simulation, and experimentally employed by Kang et al. [15] through particle sintering. Alternatively, a direct fit of the diffusivity using the extended P2D-model may be conducted, if a priori data on the particle size distribution is available. A fit with the classical P2D-model cannot reproduce the shape correctly, as the apparent diffusivity would be dependent on the chosen time frame for the relaxation fit.

B. Influence of the open circuit potential of the electrode

Both theoretical and experimental investigations suggest that the diffusion coefficient is a function of the $\mathrm{Li^+}$-loading of the electrode, therefore measurements at multiple states of charge are required [24]. Due to the results in Sections 3.2 and 4.1, it is concluded that measurement points both in rest and charge phase should be chosen within locally linear ranges of the U^{OC} curve. This reduces the deviation in the U^{OC}-gradient between particles of different sizes and therefore surface concentration, as equation (4) for the evaluation of the diffusivity assumes a constant U^{OC} derivative.

C. Relaxation time

Based on the comparison of different PSD in Section 3, it can be concluded that the necessary time for the overall equilibration correlates with the radius of the largest sized particle class, in this case R_{max}, not the mass-wise dominant fraction, R_{med}. This can be further illustrated in the comparison of the characteristic diffusion time,

$$t_{\mathrm{D}} \quad \frac{R^2}{D} \tag{9}$$

which can be used to show the discrepancy in the solid-state equilibration between median and large sized particles, Table 3. Both diffusivity and R_{med} can be found in Appendix B.

Consequently, small amounts of large particles may lead to a severe increase in the necessary relaxation time. Moreover, if consecutive experiments are conducted, as in a current- or rest phase GITT, a sequence of incomplete relaxations leads to an increasing discrepancy in the lithium content between particles of different sizes. Therefore, the composition dependent U^{OC} and reaction overpotential deviate further with each current step, leading to an increasing error in the estimation of kinetics and diffusivity. Additionally, these deviations can lead to an increased hysteresis between the analysis of charge and discharge cycles, in particular when trying to estimate the open circuit voltage.

Therefore, when designing sequential measurements, a combined procedure is advised. Preliminary simulations can be utilized to estimate the necessary duration of the relaxation period based on an approximate diffusivity coefficient. After the experiment, validation simulations using the apparent diffusion coefficient from experiments may be carried out, to estimate the accumulating error, and – if necessary – repeat the experiment with adjusted diffusion times based on intermediary values.

Furthermore, we advise the use of distinct charge/discharge phases which serve to attain the desired stoichiometry for the analysis, followed by a relaxation phase which has a duration according to the characteristic diffusion time for the 90th percentile of particle radii. This phase is then followed by the shorter GITT-current and rest phase, which only leads to a minimal change in the overall state of charge. This process is repeated for all investigated stoichiometries.

D. Current phase

Both in current and rest phase GITT, the current phase must be designed such that concentration differences between particles of different sizes are minimized. Accordingly, the electric current needs to be low, in order to minimize the effect of the varying specific surface areas of particles of different size. Furthermore, high currents increase the spatial deviations of the surface concentrations between particles, as caused by the concentration gradient in the electrolyte.

E. Limitations

While this work was exemplarily conducted on NCM-Material, the core concepts for rest phase analysis apply to other porous intercalation systems, independent of host or the type of intercalated ions. The main requirement for the application is the solid diffusion limitation of the mobile ions. Furthermore, these concepts cannot be applied to materials that exhibit pronounced phase changes and multiphase systems, such as Lithium iron phosphate cathodes. Here, Fick's law is not sufficient to describe the transport processes, and different stable or metastable phases may coexist and not exchange ions, despite concentration deviations, due to unfavorable potential [25]. This leads to constant open circuit potentials over wide ranges of charge, therefore making the evaluation of the diffusivity through GITT impossible [26,27]. Similarly, it cannot be applied to stoichiometries close to phase transitions in NCM-materials, as indicated by indentation in the U^{OC} curve and regions of nearly constant U^{OC} [28].

5. Summary and outlook

Throughout this work, the effects of non-unform particle size distributions on the rest phase behavior of Lithium-ion intercalation batteries have been investigated. We have demonstrated the interactions between particles of different sizes, and the characteristic shapes of the relaxation voltage curves. Based on this, an investigation on the deviation between the apparent and true diffusivity stemming from rest-phase GITT has been conducted, and the time-variance of the apparent diffusivity has been elucidated. This offers additional insight into the systematic discrepancy between reduced order models and experiments, as can be seen in the contributions of Horner [17] and Dees [18].

Furthermore, it has been found that the duration of the equilibration for sequential measurements needs to be chosen with respect to the largest size particles present. Hereby, the reproducibility can be improved and the charge/discharge hysteresis in GITT reduced.

Overall, these findings lead to a set of recommendations for the definition of a dedicated measurement protocol in order to decrease systematic errors of current interruption measurement and current phase measurements caused by a non-uniform particle size distributions.

List of Symbols

Name	Symbol
Greek	
Bruggeman exponent	γ
Porosity	ε
U^{OC} independent error function	E
U^{OC} independent error function derivate	E′
Reaction overpotential	η
Electronic conductivity	κ
Potential	φ
Indices	
Superscript	
Solid electrode	S
Electrolyte	E
Subscript	
Positive electrode/Cathode	P
Negative electrode/Anode	N
Separator	S
Total over all particle sizes	total
At particle center	cen
At particle surface	surf

(*continued on next column*)

(*continued*)

List of Symbols

Name	Symbol
Average over particle	av
Single particle size	SPS
Particle size distribution	PSD
Experimental values	exp
Real value	real
Apparent value	app
Particle size class	m
Latin	
Specific surface area	a
Li-Concentration	c
Diffusion coefficient	D
Potential deviation	ΔE
Faraday constant	F
Ion flux in electrolyte	i
Exchange current density	i_0
Cell current density	i_{cell}
Reaction current density	j
Overall GITT Constant	K_W
Kinetic constant	k_0
Electrode length	L
Number of particle size fractions	n_y
Ideal gas constant	R_{id}
Smallest particle size class	R_{min}
Median particle size class	R_{med}
Largest particle size class	R_{max}
Coordinate along particle radius	r
Temperature	T
Thermodynamic factor	TDF
Diffusion time	t_D
Transference number	t^0
Half-Cell Potential	U
Open circuit potential	U^{OC}
Mass fraction of a given particle size	w
Stoichiometry	x
Upper stoichiometry limit	x_{max}
Lower stoichiometry limit	x_{min}
Cell depth	Z
Coordinate along cell depth	z

CRediT authorship contribution statement

Maximilian Fath: Conceptualization, Methodology, Software, Validation, Visualization, Writing – original draft, Writing – review & editing. **Peter Heidebrecht:** Methodology, Supervision, Writing – review & editing. **Carsten Drechsler:** Conceptualization, Methodology, Writing – review & editing. **Marc Kamlah:** Supervision, Writing – review & editing.

Declaration of competing interest

The authors declare no conflict of interest.

Data availability

No data was used for the research described in the article.

Acknowledgements

This work has been supported by the German Federal Ministry for Economic Affairs and Climate Action (BMWK) under reference number 03ETE039C. The responsibility for the content of this publication lies with the author.

Furthermore, the authors acknowledge partial funding of this work by BASF SE.

This work contributes to the research performed at CELEST (Center for Electrochemical Energy Storage Ulm-Karlsruhe) and was funded by the German Research Foundation (DFG) under Project ID 390874152 (POLiS Cluster of Excellence, EXC 2154). This work was supported by

the German Research Foundation (DFG) in the framework of the research training group Simulation of Mechanical, Electrical and Thermal effects in Li-ion batteries SiMET (281041241/GRK 2218).

Appendix A. Equations of the extended P2D- Model

Table A1
Equations of the P2D Model, Adapted from Doyle [7] and Ender [11].

Equation	Description
$\frac{\partial c^{s}_{N,P}}{\partial t} \quad -\frac{1}{r_{N,P}{}^{2}}\frac{\partial}{\partial r}\left(-D^{s}_{N,P}\bullet r_{N,P}{}^{2}\bullet\frac{\partial c^{s}_{N,P}}{\partial r}\right)$	Fickian diffusion in spherical particles
$\frac{\partial \varphi^{s}_{N,P}}{\partial z} \quad \frac{i_{Cell}-i_{N,P}}{\kappa^{S}_{N,P}}$	Solid conductivity overpotential according to Ohm's Law
$i_0 \quad k_0\bullet\sqrt{(c^{s}_{max}-c^{S,surf})\bullet c^{S,surf}\bullet c^{E}}$	Exchange current density
$j_{N,P} \quad i_{0,N,P}\bullet 2\bullet\sinh\left(\frac{\eta_{N,P}\bullet F}{R_{id}\bullet T}\right)$	Reaction kinetics according to Butler-Volmer equation
$\eta_{N,P} \quad \varphi^{S}_{N,P}-\varphi^{E}_{N,P}-U^{OC}_{N,P}$	Reaction overpotential
$\varepsilon_{N,P,S}\bullet\frac{\partial c^{E}_{N,P,S}}{\partial t} \quad \frac{\partial}{\partial z}\left(D^{E}_{N,P,S}\bullet\varepsilon^{\gamma}_{N,P,S}\bullet TDF\bullet\frac{\partial c^{E}_{N,P,S}}{\partial t}\right)-\frac{1}{F}\bullet\frac{\partial(i\bullet t^{0})}{\partial z}+\frac{\sum_{m=1}^{n_y}\left(\frac{3}{r_m}\bullet w_m\right)(1-\varepsilon)\cdot j_{N,P,S}}{F}$	Salt Balance in the electrolyte
$\frac{\partial i}{\partial x} \quad \sum_{m=1}^{n_y} j_m\bullet a_m \quad \sum_{m=1}^{n_y} j_m\bullet\frac{3}{r_m}\bullet(1-\varepsilon)\bullet w_m$	Charge balance in the electrolyte for every particle class m
$\frac{\partial \varphi^{E}_{N,P,S}}{\partial z} \quad \frac{-i_{N,P,S}}{\kappa^{E}_{N,P,S}\bullet\varepsilon^{\gamma}_{N,P,S}}+\frac{2\bullet R_{id}\bullet T}{F}\bullet(1-t^{0})\bullet TDF\,\frac{1}{C}\bullet\frac{\partial c^{S}_{N,P}}{\partial z}$	Potential equation electrolyte
Boundary condition	
$\frac{\partial c^{s}_{N,P}}{\partial r}\Big\vert_{r=0} \quad 0$	Symmetrical diffusion within spherical particles
$-D^{s}_{N,P}\bullet\frac{\partial c^{s,surf}_{N,P}}{\partial r}\Big\vert_{r=R} \quad \frac{j_{N,P}}{F}$	Conservation of mass between solid and electrolyte
$\varphi^{s}_{N}\vert_{z=0} \quad 0$	Anode current collector defined as zero potential
$\varphi^{s}_{P}\vert_{z=Z} \quad U_{cell}$	Cathode current collector defined as cell voltage
$\frac{\partial c^{E}_{N}}{\partial z}\Big\vert_{z=0} \quad 0$	No concentration gradient throughout the anode current collector
$\frac{\partial c^{E}_{P}}{\partial z}\Big\vert_{z=Z} \quad 0$	No concentration gradient throughout the cathode current collector
$i_{N}\vert_{z=0} \quad 0$	No ion flux at the anode current collector
$i_{P}\vert_{z=Z} \quad 0$	No ion flux at the cathode current collector

Appendix B. Parameters of the P2D-Model

The thermodynamic factor TDF, transference number t^0, electrolyte conductivity $\kappa^{E}_{N,P}$ and the salt diffusion coefficient $D^{E}_{N,P}$ are calculated as function of the concentration according to the polynomials given by Nyman et al. [29].

The parameters of the model are taken from Chen et al. [8] unless explicitly noted, with the cathode being NCM 811, and the anode graphite/silicon blend anodes.

Name	Symbol	Units	Positive electrode	Separator	Negative electrode
Electrode length	Z	m	$75.6\bullet10^{-6}$	$12\bullet10^{-6}$	$85.2\bullet10^{-6}$
Median Particle radius	R_{med}	m	$5.22\bullet10^{-6}$		$5.86\bullet10^{-6}$
Diffusion coefficient	D	$m^2\ s^{-1}$	$1.48\bullet10^{-15}$		$1.74\bullet10^{-15}$
Cell current density	i_{cell}	$A\ m^{-2}$	13.44		
Electronic conductivity	κ	$S\ m^{-1}$	0.18		215
Faraday constant	F	$As\ mol^{-1}$			
Kinetic constant	k_0	$A\ m^{2.5}mol^{-1.5}$	$3.42\bullet10^{-6}$		$6.48\bullet10^{-7}$
Maximum Li-concentration within the solid	c^{s}_{max}	$mol\ m^{-3}$	51765		29583
Solid Stoichiometry	x	–	$\frac{c^{s}}{c^{s}_{max}}$		$\frac{c^{s}}{c^{s}_{max}}$
Stoichiometry operational maximum	x_{max}	–	0.9084		0.9014
Stoichiometry operational minimum	x_{min}	–	0.2661		0.0279
Ideal gas constant	R_{id}	$J\ K^{-1}mol^{-1}$		8.314	
Temperature	T	K	298.15		
Open circuit potential	U^{OC}	V	$fun(c^{s}_{P})$		0*
Porosity	ε	–	0.335	0.47	0.25
Bruggeman exponent	γ	–	2.43	2.57	2.91
Thermodynamic factor	TDF	–	$fun(c^{E}_{P})$	$fun(c^{E}_{P})$	$fun(c^{E}_{P})$
Transference number	t^0	–	$fun(c^{E}_{P})$	$fun(c^{E}_{P})$	$fun(c^{E}_{P})$
Area-based capacity	C	Ah/m^2		45.6	

*Modified from reference, the anode open cell potential has been set to 0.

References

[1] Z. Liu, A. Yu, J.Y. Lee, Synthesis and characterization of LiNi1−x−yCoxMnyO2 as the cathode materials of secondary lithium batteries, J. Power Sources 81–82 (1999) 416–419.

[2] S.-T. Myung, et al., Nickel-rich layered cathode materials for automotive lithium-ion batteries: achievements and perspectives, ACS Energy Lett. 2 (1) (2016) 196–223.

[3] C.-H. Lin, et al., Synthesis of micron-sized LiNi0.8Co0.1Mn0.1O2 and its application in bimodal distributed high energy density Li-ion battery cathodes, Energies 15 (21) (2022).

[4] R. Sim, et al., Influence of calendering on the electrochemical performance of LiNi(0.9)Mn(0.05)Al(0.05)O(2) cathodes in lithium-ion cells, ACS Appl. Mater. Interfaces 13 (36) (2021) 42898–42908.

[5] S. Daubner, et al., Modeling intercalation in cathode materials with phase-field methods: assumptions and implications using the example of LiFePO4, Electrochim. Acta (2022) 421.

[6] M. Wu, L. Qin, G. Wu, State of power estimation of power lithium-ion battery based on an equivalent circuit model, J. Energy Storage (2022) 51.

[7] M. Doyle, T.F. Fuller, J. Newman, Modeling of galvanostatic charge and discharge of the lithium/polymer/insertion cell, J. Electrochem. Soc. 140 (6) (1993) 1526–1533.

[8] C.-H. Chen, et al., Development of experimental techniques for parameterization of multi-scale lithium-ion battery models, J. Electrochem. Soc. 167 (8) (2020).

[9] E. Trevisanello, et al., Polycrystalline and single crystalline NCM cathode materials—quantifying particle cracking, active surface area, and lithium diffusion, Adv. Energy Mater. 11 (18) (2021).

[10] H. Buqa, et al., Behaviour of highly crystalline graphites in lithium-ion cells with propylene carbonate containing electrolytes, J. Power Sources 146 (1–2) (2005) 134–141.

[11] M. Ender, An extended homogenized porous electrode model for lithium-ion cell electrodes, J. Power Sources 282 (2015) 572–580.

[12] A. Schmidt, et al., Understanding deviations between spatially resolved and homogenized cathode models of lithium-ion batteries, Energy Technol. 9 (6) (2021).

[13] V. Laue, F. Roder, U. Krewer, Practical identifiability of electrochemical P2D models for lithium-ion batteries, J. Appl. Electrochem. 51 (9) (2021) 1253–1265.

[14] W. Weppner, R.A. Huggins, Determination of the kinetic parameters of mixed-conducting electrodes and application to the system Li3Sb, J. Electrochem. Soc. 124 (10) (2019) 1569–1578.

[15] S.D. Kang, W.C. Chueh, Galvanostatic intermittent titration technique reinvented: Part I. A critical review, J. Electrochem. Soc. 168 (12) (2021).

[16] Y.C. Chien, et al., Rapid determination of solid-state diffusion coefficients in Li-based batteries via intermittent current interruption method, Nat. Commun. 14 (1) (2023) 2289.

[17] J.S. Horner, et al., Electrochemical modeling of GITT measurements for improved solid-state diffusion coefficient evaluation, ACS Appl. Energy Mater. 4 (10) (2021) 11460–11469.

[18] D.W. Dees, et al., Analysis of the galvanostatic intermittent titration technique (GITT) as applied to a lithium-ion porous electrode, J. Power Sources 189 (1) (2009) 263–268.

[19] T.L. Kirk, C.P. Please, S. Jon Chapman, Physical modelling of the slow voltage relaxation phenomenon in lithium-ion batteries, J. Electrochem. Soc. 168 (6) (2021).

[20] J. Newmann, N.P. Balsara, Electrochemical Systems, 4. Edition ed, Wiley, Hoboken, 2021.

[21] C. Lin, A. Tang, J. Xing, Evaluation of electrochemical models based battery state-of-charge estimation approaches for electric vehicles, Appl. Energy 207 (2017) 394–404.

[22] J. Li, et al., A single particle model with chemical/mechanical degradation physics for lithium ion battery State of Health (SOH) estimation, Appl. Energy 212 (2018) 1178–1190.

[23] A. Bielefeld, et al., Influence of lithium ion kinetics, particle morphology and voids on the electrochemical performance of composite cathodes for all-solid-state batteries, J. Electrochem. Soc. 169 (2) (2022).

[24] A. Van der Ven, J. Bhattacharya, A.A. Belak, Understanding Li diffusion in Li-intercalation compounds, Acc. Chem. Res. 46 (5) (2013) 1216–1225.

[25] M. Farkhondeh, et al., Mesoscopic modeling of a LiFePO4Electrode: experimental validation under continuous and intermittent operating conditions, J. Electrochem. Soc. 164 (11) (2017) E3040–E3053.

[26] M.Z. Bazant, Theory of chemical kinetics and charge transfer based on nonequilibrium thermodynamics, Acc. Chem. Res. 46 (5) (2013) 1144–1160.

[27] Y. Zeng, M.Z. Bazant, Phase separation dynamics in isotropic ion-intercalation particles, SIAM J. Appl. Math. 74 (4) (2014) 980–1004.

[28] M. Mock, et al., Atomistic understanding of the LiNiO2–NiO2 phase diagram from experimentally guided lattice models, J. Mater. Chem. A 9 (26) (2021) 14928–14940.

[29] A. Nyman, M. Behm, G. Lindbergh, Electrochemical characterisation and modelling of the mass transport phenomena in LiPF6–EC–EMC electrolyte, Electrochim. Acta 53 (22) (2008) 6356–6365.